

Structures and Properties of Self-Assembled Monolayers of Bistable [2]Rotaxanes on Au (111) Surfaces from Molecular Dynamics Simulations Validated with Experiment

Seung Soon Jang,[†] Yun Hee Jang,[†] Yong-Hoon Kim,[†] William A. Goddard III,^{*,†} Amar H. Flood,[‡] Bo W. Laursen,[‡] Hsian-Rong Tseng,[‡] J. Fraser Stoddart,[‡] Jan O. Jeppesen,[§] Jang Wook Choi,^{||} David W. Steuerman,^{||} Erica Delonno,^{||} and James R. Heath^{||}

Contribution from the Materials and Process Simulation Center (139-74), California Institute of Technology, Pasadena, California 91125, California NanoSystems Institute and Department of Chemistry and Biochemistry, University of California, Los Angeles, 405 Hilgard Avenue, Los Angeles, California 90095-1569, Department of Chemistry, Odense University (University of Southern Denmark), Campusvej 55, DK-5230, Odense M, Denmark, and Division of Chemistry and Chemical Engineering (127-72), California Institute of Technology, Pasadena, California 91125

Received September 9, 2004; E-mail: wag@wag.caltech.edu

Abstract: Bistable [2]rotaxanes display controllable switching properties in solution, on surfaces, and in devices. These phenomena are based on the electrochemically and electrically driven mechanical shuttling motion of the ring-shaped component, cyclobis(paraquat-*p*-phenylene) (CBPQT⁴⁺) (denoted as the ring), between a tetrathiafulvalene (TTF) unit and a 1,5-dioxynaphthalene (DNP) ring system located along a dumbbell component. When the ring is encircling the TTF unit, this co-conformation of the rotaxane is the most stable and thus designated the ground-state co-conformer (GSCC), whereas the other co-conformation with the ring surrounding the DNP ring system is less favored and so designated the metastable-state co-conformer (MSCC). We report here the structure and properties of self-assembled monolayers (SAMs) of a bistable [2]rotaxane on Au (111) surfaces as a function of surface coverage based on atomistic molecular dynamics (MD) studies with a force field optimized from DFT calculations and we report several experiments that validate the predictions. On the basis of both the total energy per rotaxane and the calculated stress that is parallel to the surface, we find that the optimal packing density of the SAM corresponds to a surface coverage of 115 Å²/molecule (one molecule per 4 × 4 grid of surface Au atoms) for both the GSCC and MSCC, and that the former is more stable than the latter by 14 kcal/mol at the optimum packing density. We find that the SAM retains hexagonal packing, except for the case at twice the optimum packing density (65 Å²/molecule, the 3 × 3 grid). For the GSCC and MSCC, investigated at the optimum coverage, the tilt of the ring with respect to the normal is $\theta = 39^\circ$ and 61° , respectively, while the tilt angle of the entire rotaxane is $\psi = 41^\circ$ and 46° , respectively. Although the tilt angle of the ring decreases with decreasing surface coverage, the tilt angle of the rotaxane has a maximum at 144 Å²/molecule (the 4 × 5 grid/molecule) of 50° and 51° for the GSCC and MSCC, respectively. The hexafluorophosphate counterions (PF₆⁻) stay localized around the ring during the 2 ns MD simulation. On the basis of the calculated density profile, we find that the thickness of the SAM is 40.5 Å at the optimum coverage for the GSCC and 40.0 Å for MSCC, and that the thicknesses become less with decreasing surface coverage. The calculated surface tension at the optimal packing density is 45 and 65 dyn/cm for the GSCC and MSCC, respectively. This difference suggests that the water contact angle for the GSCC is larger than for the MSCC, a prediction that is verified by experiments on Langmuir–Blodgett monolayers of amphiphilic [2]rotaxanes.

1. Introduction

The present quest for functional nanoscale devices, such as molecular nanoelectronics^{1–3} and molecular nanomechanics,^{3–12}

[†] Materials and Process Simulation Center (139-74), California Institute of Technology.

[‡] California NanoSystems Institute and Department of Chemistry and Biochemistry, University of California.

[§] Department of Chemistry, Odense University (University of Southern Denmark).

^{||} Division of Chemistry and Chemical Engineering (127-72), California Institute of Technology.

has led to the development^{13–16} of bistable molecules such as the [2]rotaxane¹⁷ (Figure 1), which have been successfully developed into molecular machines.^{4–10} Redox-controllable [2]rotaxanes are composed of an electron-accepting cyclobis(paraquat-*p*-phenylene) (CBPQT⁴⁺ ring) that shuttles between

- (1) Reed, M. A.; Lee, T., Eds. *Molecular Nanoelectronics*; American Scientific Publishers: Stevenson Ranch, 2003.
- (2) Flood, A. H.; Ramirez, R. J. A.; Deng, W.-Q.; Muller, R. P.; Goddard III, W. A.; Stoddart, J. F. *Aus. J. Chem.* **2004**, *57*, 301–322.
- (3) Balzani, V.; Credi, A.; Venturi, M. *Molecular Devices and Machines — A Journey into the Nano World*; Wiley-VCH: Weinheim, 2003.

two electron-donating stations, such as a tetrathiafulvalene (TTF) unit and a 1,5-dioxynaphthalene (DNP) ring system when the molecular recognition affinity between the TTF donor and the CBPQT⁴⁺ acceptor is switched off and on¹⁸ by oxidizing the TTF unit to its radical cation and then reducing it back to its neutral state. The energetically favored ground-state co-conformer¹⁸ (GSCC) of the rotaxane is the one with the ring encircling the TTF unit, whereas the less-favored metastable-state co-conformer (MSCC) displays the ring on the DNP ring system. When considered as artificial molecular machinery, the salient feature of bistable rotaxanes is that the location of the ring can be controlled^{2,15–17,19,20} to encircle the TTF unit or the DNP ring system by electrochemical and electrical means and thereby inducing nanometer-scale mechanical displacement at a molecular level. Furthermore, when amphiphilic,²¹ bistable [2]rotaxanes^{12,17,19,22} are incorporated^{2,17,19} as close-packed monolayers between two-terminal electronic memory devices

they confer an ON–OFF switching behavior to the device between high and low currents. These two states are associated^{2,17} with the location of the CBPQT⁴⁺ ring. Accordingly, the GSCC of the bistable rotaxane is hypothesized to have a low conductance and is thus assigned to the OFF state of the electronic devices. The MSCC, which leads to a conductance 5–100 times larger than that of the GSCC, is found^{16,17} experimentally to decay thermally back to the GSCC. This metastable state is assigned to the device's ON state. To mimic experimentally the full device,^{2,17} a disulfide-tethered [2]rotaxane (Figure 1b) was self-assembled onto a gold electrode.²³ Electrochemical studies of this 'half device' are consistent with the mechanism of switching and the metastability observed^{2,16,17,20} in the full devices. These and other novel features of bistable [2]rotaxanes²² and bistable [2]catenanes¹⁵ lay the foundation for many new types of molecular-level devices with significant efforts focused on the generic switching behavior of molecular switches^{15–17,19,20,25–30} and molecular machines^{31–36} from solution,^{12,15,22,24a} onto surfaces^{21,23,24b} and incorporated^{16,19,20} into devices.

As a means to develop a nanotechnology based on these molecular machines, it is essential to incorporate them reliably both into integrated solid-state and "wet" devices.^{37–41} One promising means of integration is supramolecular self-organization^{42–49} harnessing interfacial, intermolecular dynamic

- (4) Barboiu, M.; Lehn, J.-M. *Proc. Natl. Acad. Sci. U.S.A.* **2002**, *99*, 5201–5206.
- (5) Hogg, L.; Leigh, D. A.; Lusby, P. J.; Morelli, A.; Parsons, S.; Wong, J. K. Y. *Angew. Chem., Int. Ed.* **2004**, *43*, 1218–1221.
- (6) Zheng, X.; Mulcahy, M. E.; Horinek, D.; Galeotti, F.; Magnera, T. F.; Michl, J. *J. Am. Chem. Soc.* **2004**, *126*, 4540–4542.
- (7) Hawthorne, F.; Zink, J. I.; Skelton, J. M.; Bayer, M. J.; Liu, C.; Livshits, E.; Baer, R.; Neuhauser, D. *Science* **2004**, *303*, 1849–1851.
- (8) de Jong, J. J. D.; Lucas, L. N.; Kellogg, R. M.; van Esch, J. H.; Feringa, B. L. *Science* **2004**, *304*, 278–281.
- (9) Turberfield, A. J.; Mitchell, J. C.; Yurke, B.; Mills, A. P.; Blakey, M. I.; Simmel, F. C. *Phys. Rev. Lett.* **2003**, *90*, 118102.
- (10) Liu, H.; Schmidt, J. J.; Bachand, G. D.; Rizk, S. S.; Looger, L. L.; Hellinga, H. W.; Montemagno, C. D. *Nature Mater.* **2002**, *1*, 173–177.
- (11) Hanke, A.; Metzler, R. *Chem. Phys. Lett.* **2002**, *359*, 22–26.
- (12) Tseng, H. R.; Vignon, S. A.; Stoddart, J. F. *Angew. Chem., Int. Ed.* **2003**, *42*, 1491–1495.
- (13) Anelli, P.-L.; Spencer, N.; Stoddart, J. F. *J. Am. Chem. Soc.* **1991**, *113*, 5131–5133.
- (14) Bissell, R. A.; Cordova, E.; Kaifer, A. E.; Stoddart, J. F. *Nature* **1994**, *369*, 133–137.
- (15) (a) Asakawa, M.; Ashton, P. R.; Balzani, V.; Credi, A.; Hamers, C.; Mattersteig, G.; Montali, M.; Shipway, A. N.; Spencer, N.; Stoddart, J. F.; Tolley, M. S.; Venturi, M.; White, A. J. P.; Williams, D. J. *Angew. Chem., Int. Ed.* **1998**, *37*, 333–337. (b) Balzani, V.; Credi, A.; Mattersteig, G.; Matthews, O. A.; Raymo, F. M.; Stoddart, J. F.; Venturi, M.; White, A. J. P.; Williams, D. J. *J. Org. Chem.* **2000**, *65*, 1924–1936.
- (16) Collier, C. P.; Mattersteig, G.; Wong, E. W.; Luo, Y.; Beverly, K.; Sampaio, J.; Raymo, F. M.; Stoddart, J. F.; Heath, J. R. *Science* **2000**, *289*, 1172–1175.
- (17) Luo, Y.; Collier, C. P.; Jeppesen, J. O.; Nielsen, K. A.; Delonno, E.; Ho, G.; Perkins, J.; Tseng, H. R.; Yamamoto, T.; Stoddart, J. F.; Heath, J. R. *ChemPhysChem* **2002**, *3*, 519–525.
- (18) Previously, we had advocated (Fyfe, M. C. T.; Glink, P. T.; Menzer, S.; Stoddart, J. F.; White, A. J. P.; Williams, D. J. *Angew. Chem.* **1997**, *109*, 2158–2160; *Angew. Chem., Int. Ed. Engl.* **1997**, *36*, 2068–2070) the use of the term *co-conformation* to designate the different three-dimension spatial arrangements of the components of mechanically interlocked molecular systems. Also, in identifying the ON and OFF states of the bistable [2]catenane employed in the first MSTJ crossbar device (see ref 16), we employed the term *co-conformer* to differentiate between the two states. See, especially Figure 1 in ref 16. In other words, in proposing our original mechanism, we appreciated correctly that the ON and OFF states are isomeric and, of course, isoelectronic.
- (19) Collier, C. P.; Jeppesen, J. O.; Luo, Y.; Perkins, J.; Wong, E. W.; Heath, J. R.; Stoddart, J. F. *J. Am. Chem. Soc.* **2001**, *123*, 12632–12641.
- (20) Diehl, M. R.; Steuerman, D. W.; Tseng, H. R.; Vignon, S. A.; Star, A.; Celestre, P. C.; Stoddart, J. F.; Heath, J. R. *ChemPhysChem* **2003**, *4*, 1335–1339.
- (21) Lee, I. C.; Frank, C. W.; Yamamoto, T.; Tseng, H.-R.; Flood, A. H.; Stoddart, J. F.; Jeppesen, J. O. *Langmuir* **2004**, *20*, 5809–5828. (b) Huang, T. J.; Tseng, H.-R.; Sha, L.; Lu, W.; Brough, B.; Flood, A. H.; Yu, B.-D.; Celestre, P. C.; Chang, J. P.; Stoddart, J. F.; Ho, C.-M. *Nano Lett.* **2004**, *4*, 2065–2071.
- (22) (a) Jeppesen, J. O.; Perkins, J.; Becher, J.; Stoddart, J. F. *Angew. Chem.* **2001**, *113*, 1251–1261; *Angew. Chem., Int. Ed.* **2001**, *40*, 1216–1221. (b) Jeppesen, J. O.; Nielsen, K. A.; Perkins, J.; Vignon, S. A.; Di Fabio, A.; Ballardini, R.; Gandolfi, M. T.; Venturi, M.; Balzani, V.; Becher, J.; Stoddart, J. F. *Chem. Eur. J.* **2003**, *9*, 2982–3007. (c) Yamamoto, T.; Tseng, H.-R.; Stoddart, J. F.; Balzani, V.; Credi, A.; Marchioni, F.; Venturi, M. *Collect. Czech. Chem. Commun.* **2003**, *68*, 1488–1514. (d) Tseng, H.-R.; Vignon, S. A.; Celestre, P. C.; Perkins, J.; Jeppesen, J. O.; Di Fabio, A.; Ballardini, R.; Gandolfi, M. T.; Venturi, M.; Balzani, V.; Stoddart, J. F. *Chem. Eur. J.* **2004**, *10*, 155–172. (e) Kang, S.; Vignon, S. A.; Tseng, H.-R.; Stoddart, J. F. *Chem. Eur. J.* **2004**, *10*, 2555–2564.
- (23) Tseng, H. R.; Wu, D. M.; Fang, N. X. L.; Zhang, X.; Stoddart, J. F. *ChemPhysChem* **2004**, *5*, 111–116.
- (24) (a) The electrochemically triggered rearrangement of an asymmetrical copper [2]catenane has been investigated kinetically by electrochemical measurements. See: Livoreil, A.; Dietrich-Buchecker, C. O.; Sauvage, J.-P. *J. Am. Chem. Soc.* **1994**, *116*, 9399–9400. (b) Although SAMs of copper catenanes have been prepared, the electrochemically triggered circumrotations are either significantly slower than the corresponding motions in solution or completely frozen out. See: Raehm, L.; Kern, J.-M.; Sauvage, J.-P.; Hamann, C.; Palacin, S.; Bourgoin, J.-P. *Chem. Eur. J.* **2002**, *8*, 2153–2162.
- (25) Credi, A.; Balzani, V.; Langford, S. J.; Stoddart, J. F. *J. Am. Chem. Soc.* **1997**, *119*, 2679–2681.
- (26) Collier, C. P.; Wong, E. W.; Belohradsky, M.; Raymo, F. M.; Stoddart, J. F.; Kuekes, P. J.; Williams, R. S.; Heath, J. R. *Science* **1999**, *285*, 391–394.
- (27) Elizarov, A. M.; Chiu, S. H.; Stoddart, J. F. *J. Org. Chem.* **2002**, *67*, 9175–9181.
- (28) Carroll, R. L.; Gorman, C. B. *Angew. Chem., Int. Ed.* **2002**, *41*, 4379–4400.
- (29) Yu, H. B.; Luo, Y.; Beverly, K.; Stoddart, J. F.; Tseng, H. R.; Heath, J. R. *Angew. Chem., Int. Ed.* **2003**, *42*, 5706–5711.
- (30) (a) Heath, J. R.; Ratner, M. A. *Phys. Today* **2003**, *56*, 43–49. (b) Flood, A. H.; Stoddart, J. F.; Steuerman, D. W.; Heath, J. R. *Science* **2004**, *306*, 2055–2056.
- (31) Balzani, V.; Gómez-López, M.; Stoddart, J. F. *Acc. Chem. Res.* **1998**, *31*, 405–414.
- (32) Balzani, V.; Credi, A.; Raymo, F. M.; Stoddart, J. F. *Angew. Chem., Int. Edit.* **2000**, *39*, 3349–3391.
- (33) Chia, S. Y.; Cao, J. G.; Stoddart, J. F.; Zink, J. I. *Angew. Chem., Int. Edit.* **2001**, *40*, 2447–2451.
- (34) Belohradsky, M.; Elizarov, A. M.; Stoddart, J. F. *Collect. Czech. Chem. Commun.* **2002**, *67*, 1719.
- (35) Hernandez, R.; Tseng, H. R.; Wong, J. W.; Stoddart, J. F.; Zink, J. I. *J. Am. Chem. Soc.* **2004**, *126*, 3370–3371.
- (36) Badjic, J. D.; Balzani, V.; Credi, A.; Silvi, S.; Stoddart, J. F. *Science* **2004**, *303*, 1845–1849.
- (37) Stoddart, J. F. *Chem. Aust.* **1992**, *59*, 576–581.
- (38) Preece, J. A.; Stoddart, J. F. *Nanobiology* **1994**, *3*, 149–166.
- (39) Gómez-López, M.; Preece, J. A.; Stoddart, J. F. *Nanotechnology* **1996**, *7*, 183–192.
- (40) Pease, A. R.; Jeppesen, J. O.; Stoddart, J. F.; Luo, Y.; Collier, C. P.; Heath, J. R. *Acc. Chem. Res.* **2001**, *34*, 433–444.
- (41) Colasson, B. X.; Dietrich-Buchecker, C.; Jimenez-Molero, M. C.; Sauvage, J. P. *J. Phys. Org. Chem.* **2002**, *15*, 476–483.
- (42) Lehn, J.-M. *Angew. Chem., Int. Ed. Engl.* **1988**, *27*, 89–112.
- (43) Lindsey, J. S. *New J. Chem.* **1991**, *15*, 153–180.
- (44) Philp, D.; Stoddart, J. F. *Synlett.* **1991**, 445–458.
- (45) Lawrence, D. S.; Jiang, T.; Levett, M. *Chem. Rev.* **1995**, *95*, 2229–2260.
- (46) Philp, D.; Stoddart, J. F. *Angew. Chem., Int. Ed. Engl.* **1996**, *35*, 1155–1196.
- (47) Seeman, N. C. *Angew. Chem., Int. Ed.* **1998**, *37*, 3220–3238.
- (48) Westhof, E.; Leontis, N. *Angew. Chem., Int. Ed.* **2000**, *39*, 1587–1591.

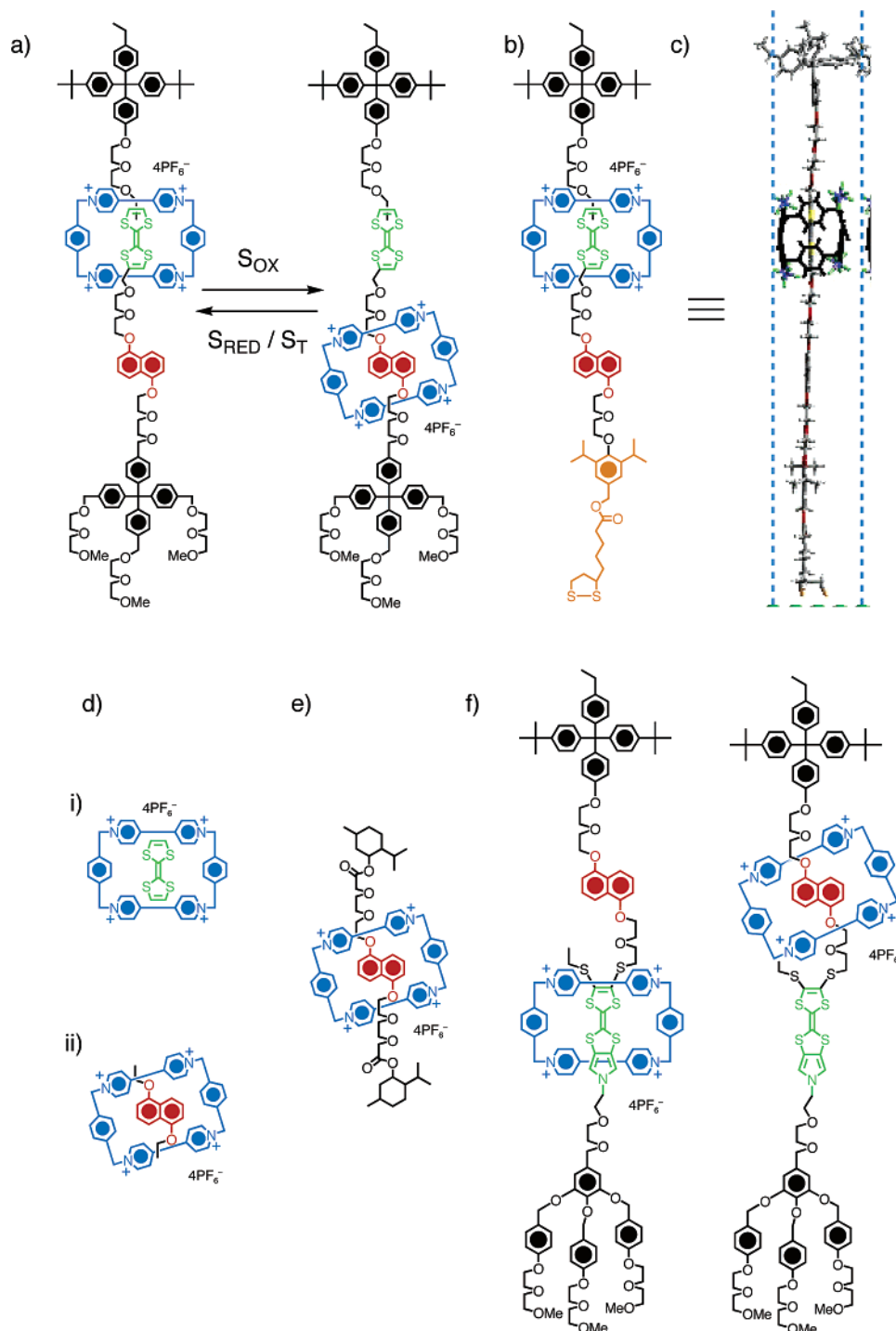


Figure 1. Bistable [2]rotaxanes based on a dumbbell-shaped component incorporating the tetrathiafulvalene unit (TTF, green) and 1,5-dioxynaphthalene ring system (DNP, red) display shuttling of a ring-shaped component, the tetracationic cyclobis(paraquat-*p*-phenylene) cyclophane (CBPQT⁴⁺, blue). (a) Amphiphilic bistable [2]rotaxanes switch between a ground-state co-conformation (GSCC), by oxidative stimulation (S_{OX}) to the metastable-state co-conformation (MSCC) and back again by reductive (S_{RED}) or thermal (S_T) stimulation. (b) Structural formula of a bistable [2]rotaxane with disulfide tethers that enables it to self-assemble on gold electrodes. (c) Graphical representation of the disulfide tethered [2]rotaxane that was used in the simulations. (d) The two 1:1 complexes between the CBPQT⁴⁺ ring and (i) tetrathiafulvalene and the (ii) 1,5-dithionaphthalene (DENP), as well as a (e) DNP-based [2]rotaxane that were utilized as computationally expedient models to optimize the force fields. (f) Amphiphilic [2]rotaxanes that are locked sterically into either the GSCC or MSCC co-conformations as isolable translational isomers.

noncovalent (and sometimes covalent bonding) interactions to form self-assembled monolayers (SAMs)^{23,24b,50} and Langmuir–Blodgett (LB)^{21,51} films on various surfaces.

Dynamic self-organized supramolecular structures designed to be thermodynamically stable provide an attractive approach

for integration—it can allow a partially damaged structure to self-heal spontaneously through the inherently dynamic properties of noncovalent bonding interactions that always drive the superstructure to reach a thermodynamically stable configuration. Indeed, nature utilizes this principle in DNA and ribosomes. In addition, even when some parts may be misconfigured, the

(49) Niemeyer, C. M.; Adler, M. *Angew. Chem., Int. Ed.* **2002**, *41*, 3779–3783.

supramolecular ensemble can retain a reliable performance by virtue of the remaining components. Moreover, practical methods for manipulating SAMs and LB films of various organic molecules are well-established.⁵²

In light of this range of benefits, studies on the self-assembly of rotaxanes^{18,19,23,50,51} are beginning to elucidate the conformations,^{21a,22e} co-conformations^{21b,50c,50f} and mechanical movements^{16,23,50c} within the monolayers. Nevertheless, the detailed characterization of the conformation of each molecule within the SAM and the intermolecular packing of these molecules are still being experimentally determined. Such structural aspects are of primary importance in designing the rotaxanes to self-organize so as to perform specific functions in a molecular electronics paradigm. Considering that the dependence of the tunneling through the rotaxane film underlying its switching behavior is a function of the molecular co-conformation^{2,3,17} (as well as the junction³⁰ between the molecule and the electrodes) of the rotaxane, a detailed knowledge of the self-organized superstructure of rotaxane within the monolayer should provide essential understanding of the fundamental nanoelectromechanical behavior of rotaxanes, allowing the molecular architecture and its packing in a device to be optimized to improve the performance of electronic and molecular devices.

Toward these goals, we report here the computed superstructures and properties of disulfide tethered bistable [2]rotaxanes²³ self-assembled on Au (111) surfaces. These studies⁵³ use fully atomistic molecular dynamics (MD) simulations to predict the superstructure of the rotaxane SAMs at 300 K as a function of surface coverage. The force field (FF) for these MD calculations is based on density functional theory (DFT) quantum mechanical (QM) calculations. Here, we described the SAM using a unit cell consisting of 16 rotaxanes over a range of different surface packing densities, from over-packed (65 Å²/molecule) to under-packed (353 Å²/molecule). Here also, we confined our inves-

tigation to the two co-conformations believed to be present in the bistable electronic device—GSCC assigned to the OFF state and MSCC assigned to the ON state—as a function of surface coverage (the study of the kinetic transition between these two states is left for future studies). In addition, we also report the experimental water contact angle measurements that validate our computations. This experiment uses LB films of amphiphilic [2]rotaxanes that are sterically locked into either the GSCC or MSCC structures. The LB films were prepared in order to characterize those surface coverages that were used in the simulations.

2. Simulation Details

To describe the intramolecular and intermolecular interactions within the film, we used the Dreiding FF,⁵⁴ which is a generic force field well tested for organic molecules. However to determine the interactions with the Au electrode, we optimized the FF parameters to fit QM calculations as discussed below.

2.1 Quantum Mechanical Calculations. All QM calculations reported here use the B3LYP^{55–58} of density functional theory (DFT) with the 6-31G**^{59–61} basis set for the organics and the LACVP**⁶² pseudopotential and basis set for Au as implemented in *Jaguar*.⁶³ We prefer the B3LYP hybrid DFT method because it leads to the most accurate thermochemistry of the various DFT methods (3.1 kcal/mol mean average discrepancy compared with the G2 database set of organic molecules).^{64–68}

2.2 Force Field and Molecular Dynamics Calculations. **2.2.1 Molecular Dynamics Parameters.** For calculations on finite molecules, no cutoffs were used for the nonbond interactions (coulomb or van der Waals). For periodic calculations, the long-range Coulomb interactions for the periodic cells used the particle–particle particle-mesh Ewald (PPPM) method.⁶⁹ The Verlet algorithm with a time step of 1.0 fs was used to integrate the equations of motion.⁷⁰ The MD calculations were of the canonical ensemble (NVT) type in which the Nose-Hoover thermostat^{71,72} (relaxation time of 0.1 ps) was used to control the temperature. The MD simulations in this study were performed using the LAMMPS (Large-scale Atomic/Molecular Massively Parallel Simulator)^{73,74} code from Sandia National Laboratories or with Cerius2 (from Accelrys).⁷⁵

- (50) (a) Kim, K.; Jeon, W. S.; Kang, J.-K.; Lee, J. W.; Jon, S. Y.; Kim, T.; Kim, K. *Angew. Chem.* **2003**, *115*, 2395–2398; *Angew. Chem., Int. Ed.* **2003**, *42*, 2293–2296. (b) Long, B.; Nikitin, K.; Fitzmaurice, D. *J. Am. Chem. Soc.* **2003**, *125*, 15490–15498. (c) Azeahara, H.; Mizutani, W.; Suzuki, Y.; Ishida, T.; Nagawa, Y.; Tokumoto, H.; Hiratani, K. *Langmuir* **2003**, *19*, 2115. (d) Hernandez, R.; Tseng, H.-R.; Wong, J. W.; Stoddart, J. F.; Zink, J. I. *J. Am. Chem. Soc.* **2004**, *126*, 3370–3371. (e) Katz, E.; Sheeney-Haj-ichia, L.; Willner, I. *Angew. Chem., Int. Ed.* **2004**, *43*, 3292–3300. (51) (a) Ahuja, R. C.; Caruso, P.-L.; Möbius, D.; Philp, D.; Preece, J. A.; Ringsdorf, H.; Stoddart, J. F.; Wildburg, G. *Thin Solid Films* **1996**, *284*, 285–671–677. (b) Amabilino, D. B.; Asakawa, M.; Ashton, P. R.; Ballardini, R.; Balzani, V.; Belohradsky, Credi, A.; Higuchi, M.; Raymo, F. M.; Shimizu, T.; Stoddart, J. F.; Venturi, M.; Yase, K. *New J. Chem.* **1998**, 959–972. (c) Asakawa, M.; Higuchi, M.; Mattersteig, G.; Nakamura, T.; Pease, A. R.; Raymo, F. M.; Shimizu, T.; Stoddart, J. F. *Adv. Mater.* **2000**, *12*, 1099–1107. (d) Brown, C. L.; Jonas, U.; Preece, J. A.; Ringsdorf, H.; Seitz, M.; Stoddart, J. F. *Langmuir*, **2000**, *16*, 1924–1930. (e) Huang, T. J.; Flood, A.; Chu, C.-W.; Kang, S.; Guo, T.-F.; Yamamoto, T.; Tseng, H.-R.; Yu, B.-D.; Yang, Y.; Stoddart, J. F.; Ho, C.-M. *IEEE-NANO* **2003**, *2*, 698–701. (52) Ulman, A. *An Introduction to Ultrathin Organic Films*; Academic Press: San Diego, 1991. (53) There have been very few computational studies on supramolecular complexes, single-molecule structures, co-conformations and switching of pseudorotaxanes, and bistable [2]catenanes and [2]rotaxanes. (a) For studies on complexation, see: Castro, R.; Davidov, P. D.; Kumar, K. A.; Marchand, A. P.; Evansek, J. D.; Kaifer, A. E. *J. Phys. Org. Chem.* **1997**, *10*, 369–382; and (b) Macias, A. T.; Kumar, K. A.; Marchand, A. P.; Evansek, J. D. *J. Org. Chem.* **2000**, *65*, 2083–2089. (c) For [2]catenanes, see: Raymo, F. M.; Houk, K. N.; Stoddart, J. F. *J. Org. Chem.* **1998**, *63*, 6523–6528. (d) For an electrochemically controllable bistable [2]rotaxane, see: Grabuleda, X.; Ivanov, P.; Jaime, C. *J. Phys. Chem. B* **2003**, *107*, 7582–7588. (e) For H-bonding [2]rotaxanes, see: Frankfort, L.; Sohlberg, K. *Theo. Chem.* **2003**, *621*, 253–260; and also, see: (f) Zheng, X.; Sohlberg, J. *Phys. Chem. A* **2003**, *107*, 1207–1215. (g) For switching in an electrochemically controllable bistable [2]catenane, see: Zheng, X.; Sohlberg, K. *PhysChemChemPhys* **2004**, *6*, 809–815.

- (54) Mayo, S. L.; Olafson, B. D.; Goddard III, W. A. *J. Phys. Chem.* **1990**, *94*, 8897–8909. (55) Becke, A. D. *Phys. Rev. A* **1988**, *38*, 3098–3100. (56) Vosko, S. H.; Wilk, L.; Nusair, M. *Can. J. Phys.* **1980**, *58*, 1200–1211. (57) Lee, C. T.; Yang, W. T.; Parr, R. G. *Phys. Rev. B* **1988**, *37*, 785–789. (58) Stephens, P. J.; Devlin, F. J.; Chabalowski, C. F.; Frisch, M. J. *J. Phys. Chem.* **1994**, *98*, 11623–11627. (59) Ditchfield, R.; Hehre, W. J.; Pople, J. A. *J. Chem. Phys.* **1971**, *54*, 724–728. (60) Hehre, W. J.; Ditchfield, R.; Pople, J. A. *J. Chem. Phys.* **1972**, *56*, 2257–2261. (61) Francl, M. M.; Pietro, W. J.; Hehre, W. J.; Binkley, J. S.; Gordon, M. S.; Defrees, D. J.; Pople, J. A. *J. Chem. Phys.* **1982**, *77*, 3654–3665. (62) Hay, P. J.; Wadt, W. R. *J. Chem. Phys.* **1985**, *82*, 299–310. (63) V. 5.0 ed.; Schroedinger Inc.: Portland, 2003. (64) Curtiss, L. A.; Raghavachari, K.; Trucks, G. W.; Pople, J. A. *J. Chem. Phys.* **1991**, *94*, 7221–7230. (65) Curtiss, L. A.; Carpenter, J. E.; Raghavachari, K.; Pople, J. A. *J. Chem. Phys.* **1992**, *96*, 9030–9034. (66) Curtiss, L. A.; Raghavachari, K.; Pople, J. A. *J. Chem. Phys.* **1995**, *103*, 4192–4200. (67) Curtiss, L. A.; Raghavachari, K.; Redfern, P. C.; Pople, J. A. *J. Chem. Phys.* **1997**, *106*, 1063–1079. (68) Koch, W.; Holthausen, M. C. *A Chemist's Guide to Density Functional Theory*; Wiley-VCH Verlag: Weinheim, 2001. (69) Hockney, R. W.; Eastwood, J. W. *Computer Simulation using Particles*; McGraw-Hill International Book Co.: New York, 1981. (70) Verlet, L. *Phys. Rev.* **1967**, *159*, 98–103. (71) Nose, S. *J. Chem. Phys.* **1984**, *81*, 511–519. (72) Hoover, W. G. *Phys. Rev. A* **1985**, *31*, 1695–1697. (73) Plimpton, S. J. *Comput. Phys.* **1995**, *117*, 1–19. (74) Plimpton, S. J.; Pollock, R.; Stevens, M. In *The Eighth SIAM Conference on Parallel Processing for Scientific Computing*; Minneapolis, 1997. (75) Accelrys Inc. *Cerius2 Modeling Environment, Release 4.0*; Accelrys Inc.: San Diego, 1999.

2.2.2 Dreiding Force Field. To allow the bistable, disulfide-tethered rotaxane to position itself optimally as a function of surface coverage, we describe all interactions using the standard Dreiding FF. Here the total potential energy is given in eq 1

$$E_{\text{total}} = E_{\text{vdW}} + E_{\text{Q}} + E_{\text{bond}} + E_{\text{angle}} + E_{\text{torsion}} + E_{\text{inversion}} \quad (1)$$

where E_{total} , E_{vdW} , E_{Q} , E_{bond} , E_{angle} , E_{torsion} , and $E_{\text{inversion}}$ are the total energies and the van der Waals, electrostatic, bond stretching, angle bending, torsion, and inversion components, respectively. The detailed parameters in the force field have been previously reported.⁵⁴

For the nonbond function we use the exponential-6 form in eq 2

$$E_{ij} = D \left[\left(\frac{6}{\zeta - 6} \right) \exp \left(\zeta \left(1 - \frac{R_{ij}}{R} \right) \right) - \left(\frac{\zeta}{\zeta - 6} \right) \left(\frac{R_{ij}}{R} \right)^{-6} \right] \quad (2)$$

Here, R_{ij} is the distance between atoms, D is the depth of the energy well, R is the distance at the energy minimum, and ζ is a dimensionless constant related to the curvature or stiffness of the inner repulsive wall (the default in Dreiding is $\zeta = 12$). The van der Waals interaction of heterogeneous atomic pairs was calculated from the geometric mean of the associated parameters of each atom. The atomic charges were assigned using the charge equilibration (QEq) method.⁷⁶

2.2.3 Validation of Dreiding Force Field for 1:1 Supramolecular Complexes. To validate the Dreiding FF for our studies, we calculated the structure and binding energies for supramolecular complexes (Figure 2) of the CBPQT⁴⁺ ring with isolated TTF⁷¹ (Figure 1di) and the analogue to DNP, 1,5-diethoxynaphthalene (DENP, Figure 1dii) using the B3LYP of DFT and Dreiding FF. These 1:1 complexes model individually the dominant noncovalent interactions of the ring with the two different recognition sites along the dumbbell of the [2]rotaxane. The binding energies for these complexes are well described (Table 1) by the Dreiding FF. Thus, the predicted free energies of binding at 300 K for the CBPQT⁴⁺ ring with TTF are 4.8 kcal/mol (QM) and 4.4 kcal/mol (FF) compared with 5.5 kcal/mol from experiment.^{78–80} The values for the complex of DENP are 2.8 kcal/mol (QM) and 2.1 kcal/mol (FF) compared with 3.9 kcal/mol from experiment.⁸¹ This leads to a difference in the binding free energy between these two supramolecular complexes of 2.0 kcal/mol (QM), 2.3 kcal/mol (FF) and 1.6 kcal/mol (experiment).^{78–81}

The predicted crystal parameters from the FF at 300 K for the complex with TTF and for the DNP-based rotaxane are in good agreement (Table 2) with experiment, and Figure 3 shows that the molecular structures within the unit cell from the simulation also match the experimental structures. Comparing analytically the structures between the FF simulation and experiment leads to coordinate root-mean-square (CRMS) differences for the TTF–CBPQT⁴⁺ complex⁸² of 0.42 Å, while for the DNP–CBPQT⁴⁺ complex,⁸³ the CRMS difference is 0.25 Å.

These results show that the standard Dreiding FF leads to a good accuracy for describing the donor–acceptor molecular recognition in

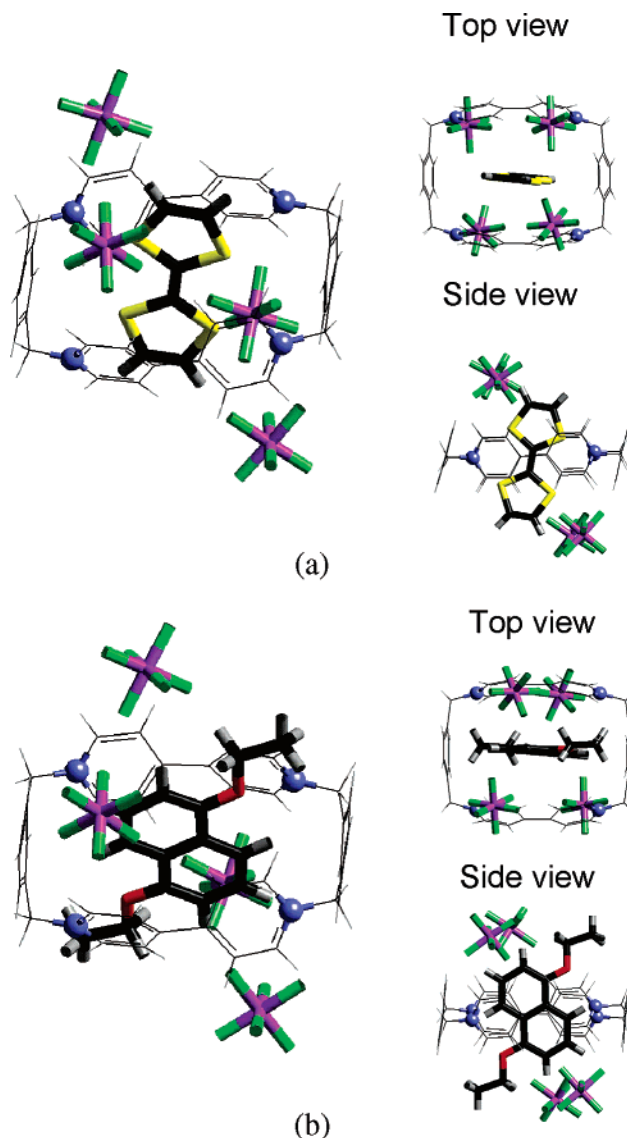


Figure 2. Simulated structures from B3LYP DFT calculations for the 1:1 complexes between the CBPQT⁴⁺ ring and (a) tetrathiafulvalene, and (b) for 1,5-diethoxynaphthalene.

this class of bistable [2]rotaxane switches. Hence, all the simulations performed on the bistable rotaxanes reported hereafter were done using the Dreiding FF integrated with the optimized Au and the Au–S force fields discussed hereafter.

2.2.4 Optimization of the Au Force Field Parameters. To determine the FF parameters for the Au–S interaction, we considered ethanethiol bonded to the Au₃₂ cluster, which is utilized to mimic the Au (111) surface. Although SAMs of alkanethiols on Au (111) have been studied intensively both experimentally^{84–100} and in computations,^{101–116} there remain many uncertainties in the structures and binding energies of alkanethiol SAMs on Au (111). Thus, the binding energies in recent computational studies using BLYP^{55,57} and PBE¹¹⁷ range from 37 to 55 kcal/mol while the recent experimental value has been reported as 30.11 kcal/mol.⁹⁵

To develop the Au–S force parameters, we considered three initial binding configurations for ethanethiol on Au₃₂ (111):

- (76) Rappe, A. K.; Goddard III, W. A. *J. Phys. Chem.* **1991**, *95*, 3358–3363.
- (77) (a) Ashton, P. R.; Philp, D.; Spencer, N.; Stoddart, J. F. *J. Chem. Soc., Chem. Commun.* **1992**, 1124–1128. (b) Anelli, P. L.; Asakawa, M.; Ashton, P. R.; Bissell, R. A.; Clavier, G.; Górski, R.; Kaifer, A. E.; Langford, S. J.; Mattersteig, G.; Menzer, S.; Philp, D.; Slawin, A. M. Z.; Spencer, N.; Stoddart, J. F.; Tolley, M. S.; Williams, D. J. *Chem. Eur. J.* **1997**, *3*, 1113–1135.
- (78) Ashton, P. R.; Balzani, V.; Becher, J.; Credi, A.; Fyfe, M. C. T.; Mattersteig, G.; Menzer, S.; Nielsen, M. B.; Raymo, F. M.; Stoddart, J. F.; Venturi, M.; Williams, D. J. *J. Am. Chem. Soc.* **1999**, *121*, 3951–3957.
- (79) Bryce, M. R.; Cooke, G.; Duclairoir, F. M. A.; Rotello, V. M. *Tetrahedron Lett.* **2001**, *42*, 1143–1145.
- (80) Nielsen, M. B.; Jeppesen, J. O.; Lau, J.; Lomholt, C.; Damgaard, D.; Jacobsen, J. P.; Becher, J.; Stoddart, J. F. *J. Org. Chem.* **2001**, *66*, 3559–3563.
- (81) Castro, R.; Nixon, K. R.; Evanseck, J. D.; Kaifer, A. E. *J. Org. Chem.* **1996**, *61*, 7298–7303.
- (82) Philp, D.; Slawin, A. M. Z.; Spencer, N.; Stoddart, J. F.; Williams, D. J. *J. Chem. Soc. Chem. Commun.* **1991**, 1584–1586.
- (83) Ashton, P. R.; Bravo, J. A.; Raymo, F. M.; Stoddart, J. F.; White, A. J. P.; Williams, D. J. *Eur. J. Org. Chem.* **1999**, 899, 9–908.

- (84) Nuzzo, R. G.; Zegarski, B. R.; Dubois, L. H. *J. Am. Chem. Soc.* **1987**, *109*, 733–740.
- (85) Dubois, L. H.; Zegarski, B. R.; Nuzzo, R. G. *Proc. Natl. Acad. Sci. U.S.A.* **1987**, *84*, 4739–4742.
- (86) Nuzzo, R. G.; Fusco, F. A.; Allara, D. L. *J. Am. Chem. Soc.* **1987**, *109*, 2358–2368.

Table 1. Energetics of Supramolecular Complexes of the CBPQT⁴⁺ Ring with TTF and DENP^a

system	energy		ZPE		ΔG (300 K)		binding free energy E_{bind} (300 K)		
	QM (Hartree)	FF (kcal/mol)	QM (kcal/mol)	FF (kcal/mol)	QM (kcal/mol)	FF (kcal/mol)	QM (kcal/mol)	FF (kcal/mol)	exp. (kcal/mol)
CBPQT ⁴⁺ & 4PF ₆ [−]	−5372.3896	−11.73	479.58	456.84	−56.35	−60.54			
TTF	−1823.7426	25.20	51.55	58.43	−22.50	−22.40			
DENP	−693.5993	12.12	180.72	179.42	−24.09	−25.59			
TTF−CBPQT ⁴⁺ & 4PF ₆ [−]	−7196.1441	−9.29	528.92	516.50	−73.97	−65.83	−4.8	−4.4	−5.5
DENP−CBPQT ⁴⁺ & 4PF ₆ [−]	−6065.9962	−18.32	656.06	636.05	−74.38	−69.29	−2.8	−2.1	−3.9

^a The binding free energies obtained by experiment for CBPQT⁴⁺ complexed with TTF are listed in refs 78–80, and for CBPQT⁴⁺ complexed with an analogue of DENP in ref 81.

Table 2. Comparison of the Unit Cell Parameters (Å) for the Crystal Structures Obtained from MD Simulations and X-ray Crystallography at 300 K

unit cell parameters	TTF−CBPQT ⁴⁺		DNP−CBPQT ⁴⁺	
	experiment ^a	dreiding FF	experiment ^b	dreiding FF
a	11.01	10.44	12.15	11.95
b	11.24	11.28	19.21	18.85
c	14.01	13.87	21.42	21.54
α	77.89	78.95	108.37	108.29
β	70.94	73.55	94.21	93.17
γ	69.91	70.14	97.33	96.02
CRMS (Å)	0.42		0.25	

^a Reference 82; *R* factor is 9.20. ^b Reference 83; *R* factor is 10.27.

(1) the sulfur (S) on a face-centered cubic (FCC) site with the carbon bonded to the S [denoted C(S)] positioned over the “on-top” site: *S*-(FCC)-C(S)(on-top);

(2) the S on FCC and C(S) positioned over hexagonal close packed (HCP) site: *S*(FCC)-C(S)(HCP);

and (3) the S on HCP and C(S) positioned over the FCC site: *S*(HCP)-C(S)(FCC).

- (87) Dubois, L. H.; Zegarski, B. R.; Nuzzo, R. G. *J. Am. Chem. Soc.* **1990**, *112*, 570–579.
- (88) Dubois, L. H.; Nuzzo, R. G. *Annu. Rev. Phys. Chem.* **1992**, *43*, 437–463.
- (89) Dubois, L. H.; Zegarski, B. R.; Nuzzo, R. G. *J. Chem. Phys.* **1993**, *98*, 678–688.
- (90) Camillone, N.; Chidsey, C. E. D.; Liu, G. Y.; Scoles, G. J. *Chem. Phys.* **1993**, *98*, 3503–3511.
- (91) Poirier, G. E.; Tarlov, M. J. *Langmuir* **1994**, *10*, 2853–2856.
- (92) Ulman, A. *Chem. Rev.* **1996**, *96*, 1533–1554.
- (93) Schessler, H. M.; Karpovich, D. S.; Blanchard, G. J. *J. Am. Chem. Soc.* **1996**, *118*, 9645–9651.
- (94) Miura, Y. F.; Takenaga, M.; Koini, T.; Graupe, M.; Garg, N.; Graham, R. L.; Lee, T. R. *Langmuir* **1998**, *14*, 5821–5825.
- (95) Lavrich, D. J.; Wetterer, S. M.; Bernasek, S. L.; Scoles, G. J. *Phys. Chem. B* **1998**, *102*, 3456–3465.
- (96) Kondoh, H.; Kodama, C.; Sumida, H.; Nozoye, H. *J. Chem. Phys.* **1999**, *111*, 1175–1184.
- (97) Tsao, M. W.; Rabolt, J. F.; Schonherr, H.; Castner, D. G. *Langmuir* **2000**, *16*, 1734–1743.
- (98) Noh, J.; Hara, M. *Langmuir* **2002**, *18*, 1953–1956.
- (99) Noh, J.; Hara, M. *Langmuir* **2002**, *18*, 9111–9115.
- (100) Kato, H. S.; Noh, J.; Hara, M.; Kawai, M. *J. Phys. Chem. B* **2002**, *106*, 9655–9658.
- (101) Hautman, J.; Klein, M. L. *J. Chem. Phys.* **1989**, *91*, 4994–5001.
- (102) Hautman, J.; Bareman, J. P.; Mar, W.; Klein, M. L. *J. Chem. Soc., Faraday Trans.* **1991**, *87*, 2031–2037.
- (103) Sellers, H.; Ulman, A.; Shnidman, Y.; Eilers, J. E. *J. Am. Chem. Soc.* **1993**, *115*, 9389–9401.
- (104) Mar, W.; Klein, M. L. *Langmuir* **1994**, *10*, 188–196.
- (105) Gerdy, J. J.; Goodard III, W. A. *J. Am. Chem. Soc.* **1996**, *118*, 3233–3236.
- (106) Beardmore, K. M.; Kress, J. D.; Gronbeck-Jensen, N.; Bishop, A. R. *Chem. Phys. Lett.* **1998**, *286*, 40–45.
- (107) Li, T. W.; Chao, I.; Tao, Y. T. *J. Phys. Chem. B* **1998**, *102*, 2935–2946.
- (108) Groenbeck, H.; Curioni, A.; Andreoni, W. *J. Am. Chem. Soc.* **2000**, *122*, 3839–3842.
- (109) Andreoni, W.; Curioni, A.; Groenbeck, H. *Int. J. Quantum Chem.* **2000**, *80*, 598–608.
- (110) Hayashi, T.; Morikawa, Y.; Nozoye, H. *J. Chem. Phys.* **2001**, *114*, 7615–7621.
- (111) Akinaga, Y.; Nakajima, T.; Hirao, K. *J. Chem. Phys.* **2001**, *114*, 8555–8564.
- (112) Vargas, M. C.; Giannozzi, P.; Selloni, A.; Scoles, G. J. *Phys. Chem. B* **2001**, *105*, 9509–9513.
- (113) Yourdshahyan, Y.; Zhang, H. K.; Rappe, A. M. *Phys. Rev. B* **2001**, *63*, 081405.
- (114) Krueger, D.; Fuchs, H.; Rousseau, R.; Marx, D.; Parrinello, M. *J. Chem. Phys.* **2001**, *115*, 4776–4786.
- (115) Zhang, L. Z.; Goodard III, W. A.; Jiang, S. Y. *J. Chem. Phys.* **2002**, *117*, 7342–7349.
- (116) Tachibana, M.; Yoshizawa, K.; Ogawa, A.; Fujimoto, H.; Hoffmann, R. *J. Phys. Chem. B* **2002**, *106*, 12727–12736.

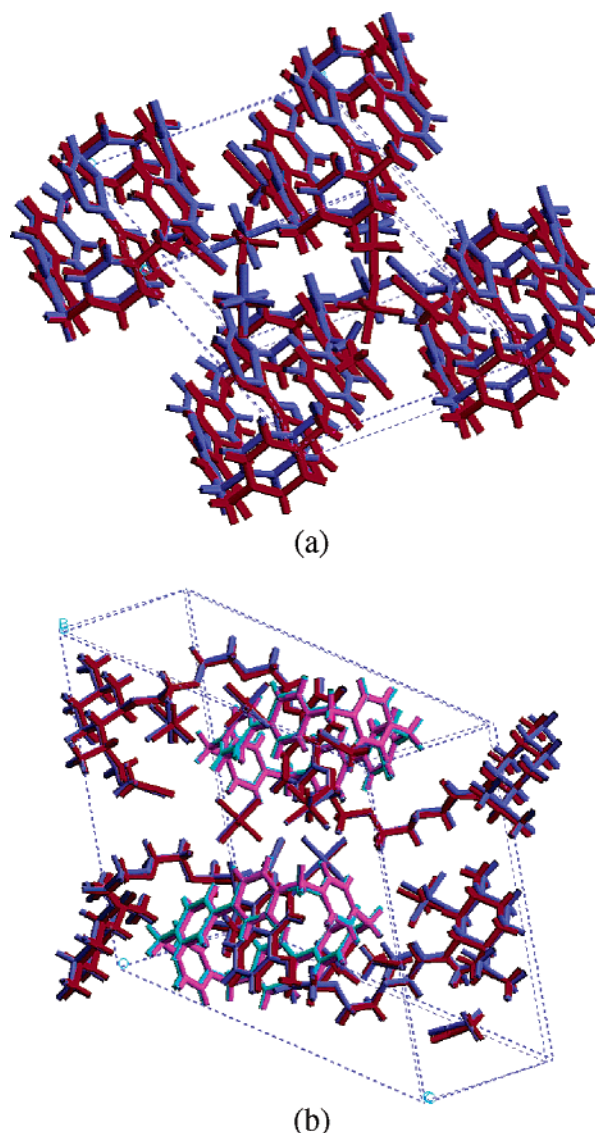


Figure 3. (a) Comparison of the calculated and experimental crystal structures of the 1:1 complex between CBPQT⁴⁺ and TTF (calculation in blue and experimental in red) showing all four molecules in the unit cell, and (b) same comparison for the DNP-based [2]rotaxane.

Here, FCC indicates the 3-fold site beneath which there is no Au atom in the second layer but with an Au atom (red color) in the third

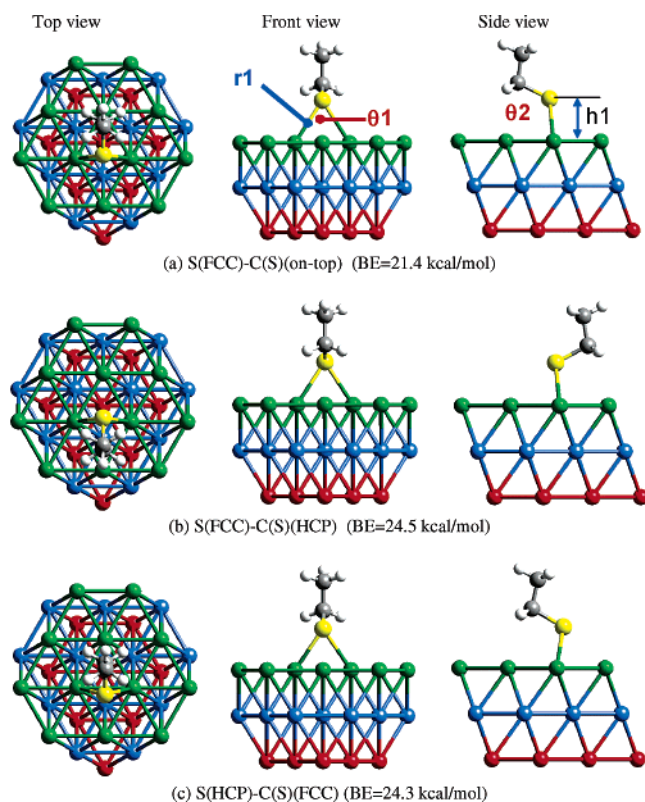


Figure 4. Optimized geometries of the ethanethiol-Au₃₂ cluster (yellow S, gray C, white H, green Au (first layer), blue Au (second layer), red Au (third layer)). (a) S(FCC)-C(S) (on-top), with a binding energy (BE) of 20.3 kcal/mol; (b) S(FCC)-C(S)(HCP) (BE = 24.5 kcal/mol); and (c) S(HCP)-C(S)(FCC) (BE = 24.3 kcal/mol). Starting with either types of 3-fold site leads to a 2-fold final structure, indicating that the thiol S prefers to binds to a pair of surface Au atoms.

layer, while HCP denotes the 3-fold site above which there is a Au atom (blue color) in the second layer. In each case the optimized molecular structure leads to a situation with the sulfur atom of ethanethiol located (Figure 4) near the bridge site between two Au atoms (S-Au distances of 2.634 Å). This positioning of the sulfur at the bridge site has also been observed in recent PBE and BLYP^{110–112} calculations on Au (111) slabs.

We find (Table 3) that the most stable conformation is the S(FCC)-C(S)(HCP) with a net binding energy of 24.53 kcal/mol. The other two sites are higher by 4.30 kcal/mol [S(FCC)-C(S)(on top)] and 0.26 kcal/mol [S(HCP)-C(S)(FCC)]. These computed values can be compared to the recent experimental value (30.11 kcal/mol).⁹⁵

We used the QM geometry and binding energy to fit the FF parameters for the Au-S interaction obtaining (see Table 4) $D = 9.033$ kcal/mol and $R = 2.682$ Å ($z = 12$ was kept at the default value) by assuming the geometric mean combination rules for other heterogeneous atomic pair of Au (from the universal FF¹¹⁸) with an atom in the organic molecule, such as, C and H (from Dreiding FF).⁵⁴ Here, it should be addressed that the binding energy for ethanethiol-Au lies in the range of 20–30 kcal/mol and the S-Au distance is of the order of 2.6–2.7 Å which is much closer to the sum of their respective atomic radii than to the sum of their van der Waals radii. This is because the bond characteristics between S-Au is a chemical bond rather than a physical bond.

For the bulk Au FF, we used the same exponential-6 type function as for the organic-Au interactions in eq 2. These parameters were optimized to fit the experimental bulk properties of Au (see Table 5)

such as density, heat capacity and the crystal cell parameters. It should also be pointed that this FF parameters for the bulk Au (used in the exponential-6 function) is not for the van der Waals interaction, but for the metallic bond interaction. For this reason, we adopted the Universal FF Au parameter for the off-diagonal van der Waals interaction between Au and the rest of element (different from S).

3. Results

3.1 Molecular Dynamics Simulation of Rotaxane SAM.

To predict the most probable structure of the rotaxane SAMs on Au (111) surfaces, we constructed SAMs with various surface coverages for both co-conformations of the bistable rotaxane:

- with the ring encircling the TTF unit (GSCC)
- with the ring encircling the DNP unit (MSCC)

Starting with the unit surface of Au (111) (the 1×1 grid) (Figure 5a), we constructed various a $m \times n$ super-cells as shown in Figure 5b. We placed a fully extended rotaxane within the supercell on top of each surface and conducted a canonical ensemble (NVT) MD simulation at 300 K for 100 ps to preequilibrate the system. Figure 6a illustrates the case for the GSCC on the 4×4 grid of the Au (111) surface. This preequilibration allows the molecular conformation to relax and fold. Of course this molecule interacts with the whole monolayer of other rotaxanes. Consequently, we constructed superstructures consisting of 16 rotaxanes, using these preequilibrated single molecular systems (Figure 6b shows the superstructure based on the 4×4 grid/molecule) and equilibrated them with 1 ns NVT MD at 300 K. Finally, we performed another 2 ns NVT MD simulation at the same temperature in order to collect the statistics of structures and energetics of the rotaxane SAMs.

3.2 SAM Formation Energy. From the equilibrium NVT MD simulations for the superstructures with various surface coverages, we calculated the SAM formation energy (E_{SAM}) defined in eq 3 to evaluate their stability.

$$E_{\text{SAM}} = \frac{E_{\text{total}} - (E_{\text{Au}} + n \times E_{\text{single rotaxane}})}{n} \quad (3)$$

where E_{total} is the total energy of the system, E_{Au} and $E_{\text{single rotaxane}}$ is the energy of a bare Au (111) surface and of a single rotaxane molecule in the gas phase, respectively. Here, n denotes the number of rotaxane molecules, which is 16 for all the systems studied here. E_{SAM} is the average cohesive energy for the SAM on the Au (111) surface, using the GSCC and MSCC in the gas phase as the reference points. More negative values of E_{SAM} correspond to greater SAM stability. Figure 7 shows the dependence of E_{SAM} on the surface area/molecule. We see that the GSCC is more stable than the MSCC by ~ 14 kcal/mol over all ranges of the surface area/molecule surveyed. This computed value can be compared to the difference in the isolated rotaxane of only 2.0 kcal/mol. Thus, the difference in packing of the GSCC versus the MSCC is 12 kcal/mol (for the 4×4 grid/molecule best case).

The stability of the GSCC over the MSCC has been confirmed on all occasions by experiment.^{2,16,17,20,23} Thus, the GSCC is observed as the equilibrium co-conformation for both half and full devices. For the half-device, the observation²³ is that, once the MSCC is formed it relaxes back to the ground-state over a period of ~ 1 s when the positive bias is removed. Similarly, in the electronic devices the metastable state that is once again assigned to the MSCC relaxes^{2,17} back to the ground-state one

(117) Perdew, J. P.; Burke, K.; Ernzerhof, M. *Phys. Rev. Lett.* **1996**, *77*, 3865–3868.

(118) Rappe, A. K.; Casewit, C. J.; Colwell, K. S.; Goddard, W. A.; Skiff, W. M. *J. Am. Chem. Soc.* **1992**, *114*, 10024–10035.

Table 3. Energetics for Ethanethiol on Au₃₂ (111) with Their Corresponding Spin States

system	energy (Hartree)
components	<div> <div>SCH₂CH₃</div> <div>Au₃₂</div> </div> <div> <div>−4336.10353</div> <div>(<i>S</i> = 0)</div> </div> <div> <div>−477.38230 (<i>S</i> = 1/2)</div> <div>−4336.10475</div> <div>(<i>S</i> = 1)</div> <div>−4336.09099</div> <div>(<i>S</i> = 2)</div> </div>
SCH ₂ CH ₃ on Au ₃₂ (111) (<i>S</i> = 1/2)	<div>−4813.51930 (<i>S</i> = 1/2)</div> <div>−4813.51312 (<i>S</i> = 3/2)</div> <div>−4813.52572 (<i>S</i> = 1/2)</div>
binding energy	<div>20.23 (kcal/mol)</div> <div>24.53 (kcal/mol)</div> <div>24.27 (kcal/mol)</div>

Table 4. Optimized Force Field Parameters for the Interaction between Au and Organic Molecules and Comparison of the Geometry and Binding Energy with QM

	<i>D</i> (kcal/mol)	<i>R</i> (Å)	<i>z</i>
Au–S	9.033	2.682	12.0
Au–C ^a	0.064	3.561	12.0
Au–H ^a	0.041	3.082	12.0
Au–N ^a	0.052	3.472	12.0
Au–O ^a	0.048	3.395	12.0
Au–P ^a	0.112	3.697	12.0
Au–F ^a	0.045	3.337	13.4

SCH ₂ CH ₃ -on-Au ₃₂ (111)			
S(FCC)–C(S)(HCP)		quantum	force field
binding energy (kcal/mol)		−24.53	−24.53
geometry ^b	<i>r</i> 1 (Å)	2.634	2.634
	<i>h</i> 1 (Å)	2.199	2.058
	<i>θ</i> 1 (deg)	66.4	66.4
	<i>θ</i> 2 (deg)	112.9	110.2

^a These parameters were determined by geometric mean of Au parameter in Universal FF¹¹⁸ and each atom parameters in Dreiding FF.⁵⁴ ^b See Figure 4a for definition of the geometric variables.

Table 5. Force Field Parameters for Au Optimized to Fit the Properties of the FCC Crystal

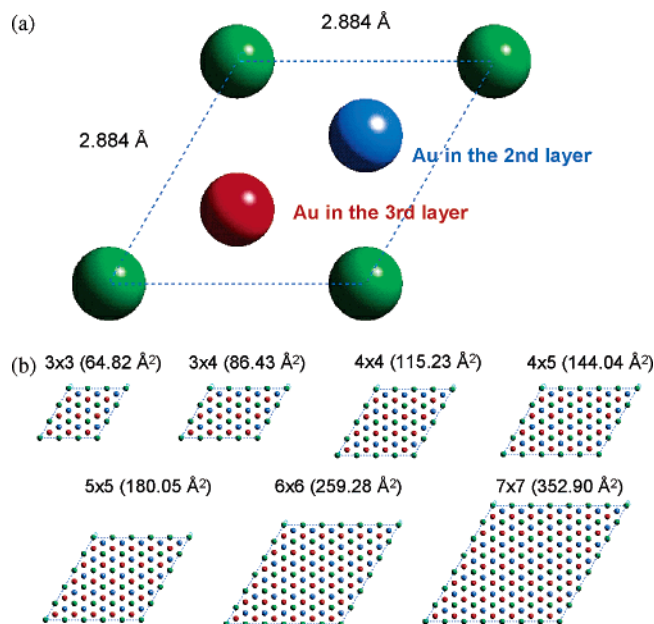
<i>D</i> (kcal/mol)	<i>R</i> (Å)	<i>z</i>
3.035	2.993	12.0

properties (300 K)	experimental	simulation ^a
density (g/cm ³)	19.32	19.35
Δ <i>H</i> _(300 K – 0 K) (kcal mol ^{−1})	1.447	1.447
<i>C</i> _p (cal/mol K)	6.078	5.611
cell parameters	<i>a</i> = <i>b</i> = <i>c</i> = 4.0782 Å	<i>a</i> = <i>b</i> = <i>c</i> = 4.0763 Å
of the crystal	<i>a</i> = <i>b</i> = <i>g</i> =90 °	<i>a</i> = <i>b</i> = <i>g</i> =90 °
Au–Au distance (Å)	2.884	2.882

^a The simulations for Au crystal used a 5 × 5 × 5 Brillouin zone to calculate the phonon spectra used for the thermochemical properties. The unit cell consisted of 256 Au atoms

over a period of ~10 min when the external +2 V positive bias applied to the bottom electrode—mimicked by the Au (111) surface in this study—is removed. Although we have not observed this dynamic shuttling motion of the CBPQT⁴⁺ ring from the DNP ring system to the TTF unit within several nanoseconds of simulation, we have validated that the energetics of these two distinct co-conformations are properly described in our simulation.

We find that both co-conformations lead to the most stable monolayer for a surface packing density of 115 Å²/molecule corresponding to the superstructure generated (Figure 6b) from the 4 × 4 grid/molecule. This is 14.9 kcal/mol more stable than the 3 × 4 (65 Å²/molecule) SAM and 8.8 kcal/mol more stable than the 4 × 5 (144 Å²/molecule) SAM. Depending on the experimental conditions for the formation of the SAM, it is

**Figure 5.** Top views of (a) the unit surface of Au (111) (1 × 1) and of (b) *n* × *m* Au (111) surfaces with various areas.

possible that other surface coverages might be observed due to the small energy differences between each of them.

3.3 Structure of the Rotaxane SAMs. Next, we analyze how the rotaxanes are packed in a SAM at various surface coverages. Since the switching behavior in electronic devices incorporating rotaxanes is believed to result from shuttling of the CBPQT⁴⁺ ring between the TTF unit and DNP ring system, it is important to understand the superstructure of the SAM in both of these equilibrated co-conformations.

3.3.1 Packing and Tilt. Figure 8 shows the packing of CBPQT⁴⁺ rings in the SAM with various surface coverages—the remaining parts of the rotaxane were removed for clarity. For both the GSCC and MSCC, we find that the rotaxanes retain hexagonal packing over the 2 ns NVT MD simulation. The exception is the over-packed SAM using the 3 × 3 grid/molecule, where steric interactions between the CBPQT⁴⁺ rings on neighboring rotaxanes cause a very unstable structure with disordered layers (Figure 8).

For the lower surface coverages, such as the 6 × 6 grid/molecule (260 Å²/molecule), we find that the CBPQT⁴⁺ rings are parallel to the surface (Figure 8). We would expect that this type of packing would be best for switching since the ring could shuttle along the dumbbell without changing the intermolecular interactions significantly between the GSCC and MSCC.

The differences in orientation of the ring for different packing densities are reflected in an increase in the average tilt as the

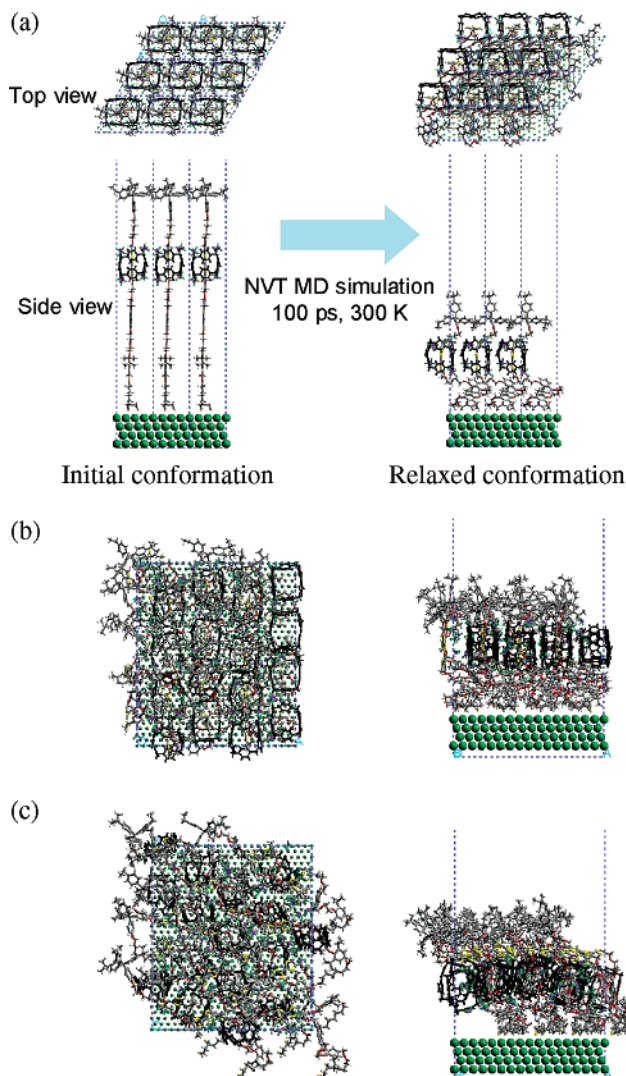


Figure 6. Initial and optimum structures (a) for the GSCC using a 4×4 grid of Au surface atoms per unit cell. One independent molecule per 4×4 unit cell, 9 such cells are shown here. Starting with the optimum structure obtained from (a), we constructed the 4×4 supercell consisting of 16 rotaxanes (b) for the GSCC and, similarly, (c) for the MSCC and subsequently allowed each of the rotaxanes to equilibrate independently for 1 ns, leading to the structures shown.

surface coverage increases. To quantify this observation, we define the tilt angle θ of the ring (Figure 9a) as the angle between the vector perpendicular to the plane of the ring, \mathbf{n}_{ring} , and the normal Au (111) surface, $\mathbf{n}_{\text{surface}}$. Thus, for coverages below $353 \text{ \AA}^2/\text{molecule}$ (the 7×7 grid/molecule), the rotaxanes accommodate increased surface coverage by increasing (Figure 9b) the average tilt of the CBPQT⁴⁺ ring (Figure 9b). However, the value of the tilt angle is $\sim 20^\circ$ larger for the MSCC than for the GSCC—except for the largest surface area case, the 7×7 grid/molecule. This greater tilt for the CBPQT⁴⁺ ring is required in order to encircle the DNP ring system which is at an angle with respect to the rotaxane axis, whereas (Figure 4) the TTF unit is not.

We also analyzed the tilt (ψ) of the dumbbell component of the rotaxane. It is ambiguous to define the tilt angle of a highly flexible and folded molecule such as the rotaxane. Consequently, we calculated the moment of inertia tensor and defined the tilt with respect to the longest principal axis (smallest moment of inertia). As shown in Figure 10, the tilt angle of the rotaxane is

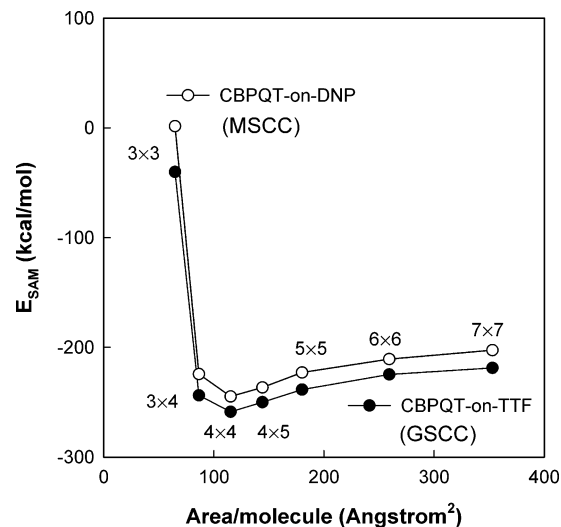


Figure 7. The binding energy per rotaxane for SAMs with various surface areas. Here the reference point is the free surface and the free optimized molecule. The optimum coverage for both cases is the 4×4 case. Here, the @TTF (the GSCC) structure is more stable by 14 kcal/mol than @DNP (the MSCC).

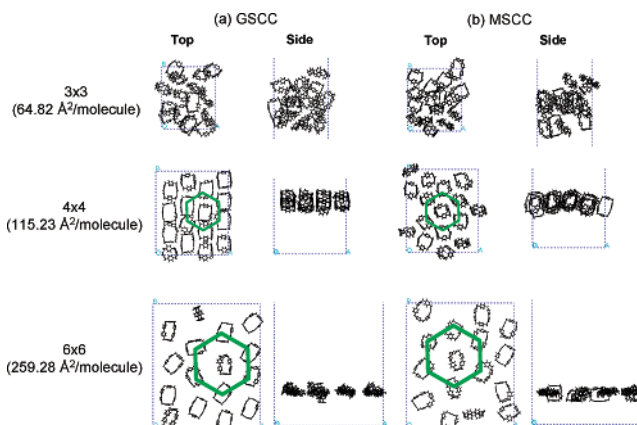


Figure 8. Optimized packing of CBPQT⁴⁺ rings for SAMs with various surface coverages. In each case there were 16 rotaxanes per unit cell. Here, we show just the rings for clarity of the (a) GSCC and (b) MSCC. The approximate closest packing is shown by the green hexagons. This shows that the 3'3 packing leads to a second layer of rings.

at a maximum ($\sim 50^\circ$) for the 4×5 grid/molecule ($144 \text{ \AA}^2/\text{molecule}$). The relation between tilt angle and the dumbbell's conformation is represented graphically in the insets shown in Figure 10. At the highest surface coverages (smallest area/molecule), the conformation of the whole dumbbell component is extended and standing vertically. As the area/molecule increases, the rotaxane starts tilting down. As sufficient space on the surface becomes available, the tilt angle starts decreasing toward smaller values ($10\text{--}20^\circ$). At these surface coverages, each rotaxane has enough room to fold down (Figure 10c) leading to a shorter albeit more vertical principal axis.

3.2.2 Density Profile. The previous section reported the packing-dependent structure of individual rotaxanes. In this section, we examine the mass density distribution. These are potentially measurable quantities and they provide useful insight into the properties of nanoscale layers. In particular, it is useful to determine how these properties relate to the spatial distribution of the CBPQT⁴⁺ ring component. For example, how does the thickness of the SAM change as the location of the CBPQT⁴⁺ ring is switched from the TTF unit to the DNP

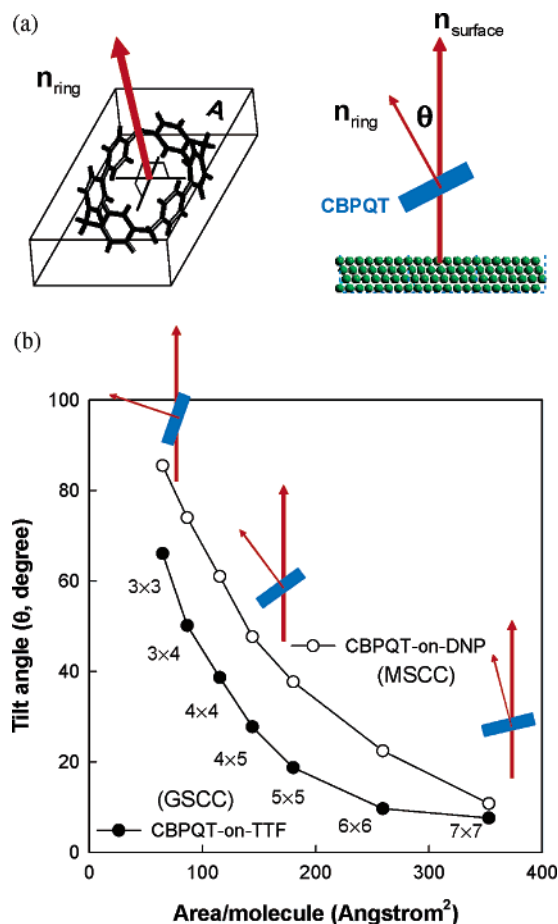


Figure 9. (a) Definition of the tilt angle (θ) of the CBPQT⁴⁺ ring and (b) the dependence of the tilt angle on the area per molecule, averaged over all 16 independent rotaxanes for both co-conformations.

ring system? We analyzed the density profiles by slicing (Figure 11) the system into 1.5 Å slabs parallel to the Au (111) surface (XY plane). The density profiles of each system along the direction perpendicular to the surface (Z-axis) in the simulation box were obtained by averaging the mass densities of each slab over the entire MD simulation.

Figure 12 shows how the surface coverages affect the overall density profiles, as well as the distribution of the CBPQT⁴⁺ ring and its hexafluorophosphate counterions (PF₆[−]) for both co-conformations. Defining the top of the SAM as the highest slab at which the density has a nonzero value, we see that the most stable SAM has a thickness of ~40 Å for both co-conformations. This conclusion may be important for device fabrication where an absence of significant dimensional changes before and after the shuttling motion of the CBPQT⁴⁺ ring aids in switching of the rotaxane SAMs. At the higher surface coverages (small area/molecule), the rotaxanes stand in the extended conformation, so that the height of the SAM is greatest, whereas, the molecules are folded and dispersed on the surface at low surface coverages (large area/molecule), leading to a thin monolayer.

We find that the four counterions (PF₆[−]) remain associated with the CBPQT⁴⁺ ring during the entire 3 ns MD simulations. Given the correlation between the location of the counterions and the ring we expect that the counterions are likely to follow the CBPQT⁴⁺ ring when it shuttles between the two stations (TTF and DNP).

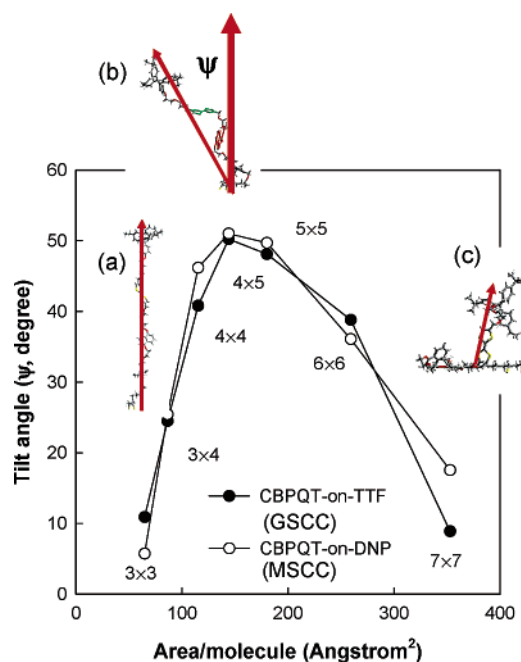


Figure 10. Change in the tilt angle (ψ) of the entire rotaxane backbone for both co-conformations as a function of the area/molecule. Graphical representations of the dumbbell component of the (a) 3 × 3, (b) 4 × 5, and (c) 7 × 7 grids illustrate the actual conformations of the dumbbell component.

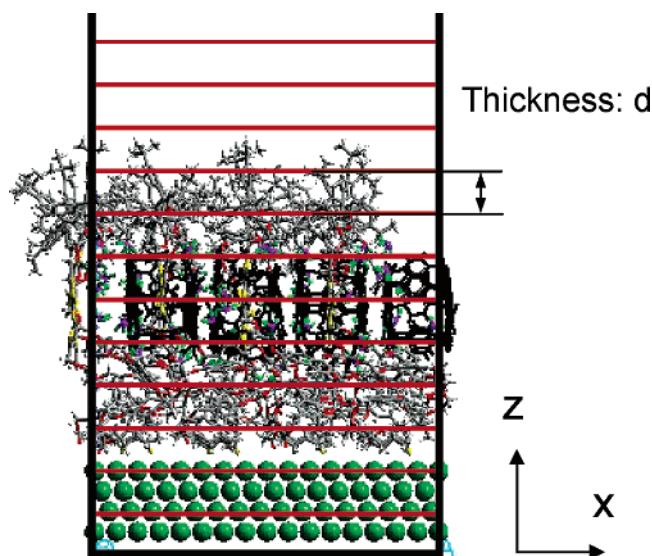


Figure 11. Graphical representation of how the systems were sliced into slabs of thickness d in order to calculate the density and stress. In this study, we used $d = 1.5$ Å.

3.2.3 Stress Analysis. In a manner that is similar to the density profile analysis, we also analyzed the stress distribution in the SAM perpendicular to the Au (111) surface (Z-axis) at each surface coverage using the Kirkwood–Buff theory¹¹⁹

$$P_N(z) = \rho(z)k_B T - \frac{1}{V_{\text{slab}}} \left\langle \sum_{ij} \frac{z_{ij}^2}{r_{ij}} \frac{du(r_{ij})}{dr_{ij}} \right\rangle \quad (4)$$

$$P_T(z) = \rho(z)k_B T - \frac{1}{V_{\text{slab}}} \left\langle \sum_{ij} \frac{x_{ij}^2 + y_{ij}^2}{2r_{ij}} \frac{du(r_{ij})}{dr_{ij}} \right\rangle \quad (5)$$

where $P_N(z)$ and $P_T(z)$ are the normal and tangential compo-

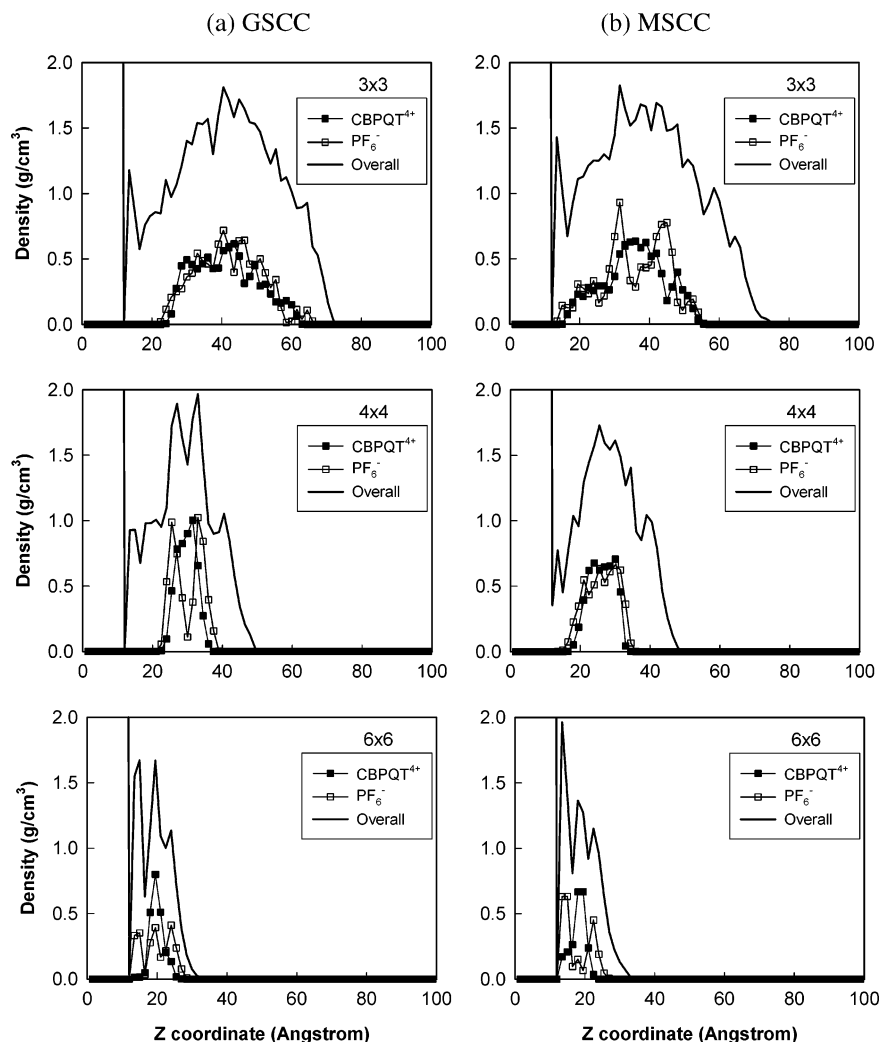


Figure 12. Mass density profiles for the (a) GSCC and (b) MSCC of the overall SAM, the CBPQT⁴⁺ ring and the PF₆[−] anions as a function of surface coverage. Here $Z = 10$ corresponds to the Au surface atoms.

nents of the stress of the slab at z . $\rho(z)$ and V_{slab} denote the density of the slab at z and the slab volume, respectively, and k_B and T are the Boltzmann constant and the absolute temperature, respectively. Angle brackets mean an ensemble average of all atoms located in the slab at z . r_{ij} , x_{ij} , y_{ij} , and z_{ij} are the distance between atoms and its coordinate components, respectively, and $u(r_{ij})$ is the potential energy of the atomic pair i and j . This theory has been used successfully to study the complicated interface mediated by surfactant molecules¹¹² as well as the liquid/vapor interface.^{113–121}

Figure 13 shows how the stress in the SAM is distributed as a function of the surface coverage for the two co-conformations. We observe that for the most stable SAM, with 4×4 grid/molecule, both the GSCC and MSCC have a more relaxed stress state than the other surface coverages. The 3×3 grid/molecule case, which was found to be quite unstable, has positive stress in $P_T(z)$ ranging over the region 20–50 Å away from the surface for the MSCC. This indicates that this SAM structure tends to expand laterally because it is too crowded. By contrast, the

component of $P_N(z)$ has little positive stress since the structure can access relaxation pathways by swelling along the Z -axis direction. On the other hand, the 6×6 grid/molecule case has negative stress values within the SAM, for both $P_T(z)$ and $P_N(z)$, which indicates that the SAM tends to shrink in all directions. At these low surface coverages, the attractive interaction inside the SAM wants to increase to reach optimal packing. These studies show that neither the over-packed (3×3) nor the under-packed (6×6) SAM is stable from the viewpoint of the stress state, which is consistent with the SAM formation energy analysis.

3.2.4 Surface Tension. The surface tension of the SAM at each surface coverage was calculated using the mechanical definition of surface tension.^{130,131}

$$\gamma = \int_{L_1}^{L_2} dz [P_N(z) - P_T(z)] \quad (6)$$

where L_1 and L_2 set the integration range, which in this case, is defined by the thickness of the SAM along the Z -axis direction.

For the optimal packing condition (the 4×4 grid/molecule), the value of the surface tension is predicted (Table 6) to be 45

(119) Kirkwood, J. G.; Buff, F. P. *J. Chem. Phys.* **1949**, *17*, 338–343.

(120) Jang, S. S.; Lin, S.-T.; Maiti, P. K.; Blanco, M.; Goddard III, W. A.; Shuler, P.; Tang, Y. *J. Phys. Chem. B* **2004**, *108*, 12130–12140.

(121) Freeman, K. S. C.; McDonald, I. R. *Mol. Phys.* **1973**, *26*, 529–537.

(122) Rao, M.; Levesque, D. *J. Chem. Phys.* **1976**, *65*, 3233–3236.

(123) Miyazaki, J.; Barker, J. A.; Pound, G. M. *J. Chem. Phys.* **1976**, *64*, 3364–3369.

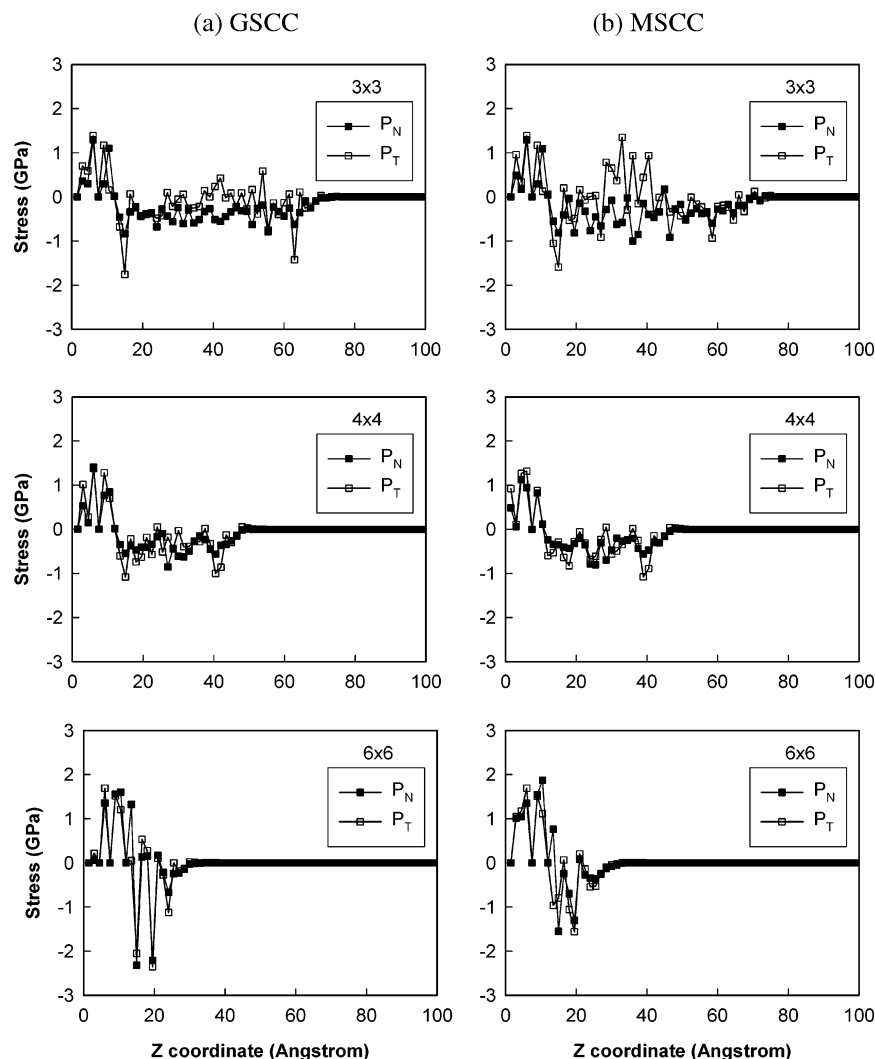


Figure 13. Stress profiles normal to the film (P_N) and in the plane of the film (P_T) at various surface coverages for the (a) GSCC and the (b) MSCC.

dyn/cm for the GSCC, and 65 dyn/cm for the MSCC. This difference in the surface tension suggests that the SAM of the GSCC is more hydrophobic than for the MSCC. This implies that the water contact angle of the SAM for the GSCC should be significantly larger than that for the MSCC.

To confirm this prediction, we measured experimentally the water contact angle on LB films of two amphiphilic [2]rotaxanes (Figure 1f) across a range (Table 6) of surface coverages. These

Table 6. Comparison of the Experimental Water Contact Angle from Langmuir–Blodgett Films of Amphiphilic Rotaxanes¹³² with the Surface Tension from MD Simulations of Rotaxane SAMs at 300 K

area/molecule (\AA^2)	experimental water contact angle (deg) ^a	
	GSCC	MSCC
120	85 ± 2	76 ± 2
165	79 ± 1	70 ± 1
240	72 ± 1	57 ± 2

area/molecule (\AA^2)	simulated surface tension (dyn/cm)	
	GSCC	MSCC
66 (3×3)	−960.75	−1483.27
86 (3×4)	−434.49	−657.43
115 (4×4)	44.50	65.42
144 (4×5)	51.79	69.10
180 (5×5)	54.53	73.65
260 (6×6)	64.58	86.60
353 (7×7)	68.71	90.52

^a The contact angles were measured from the completely dried LB film transferred from Langmuir monolayer on water onto nonpatterned substrate of identically cleaned glass slide, using H_2O (18.2 megaohms, milipure).

[2]rotaxanes are locked sterically into either the GSCC or MSCC by means of an ethyl group. They are amphiphilic, which allows for LB monolayers to be transferred to glass substrates at different surface coverages. We found that, for the same area/

- (124) Rao, M.; Berne, B. J. *Mol. Phys.* **1979**, *37*, 455–461.
 (125) Nicolas, J. P.; Smit, B. *Mol. Phys.* **2002**, *100*, 2471–2475.
 (126) Chapela, G. A.; Saville, G.; Thompson, S. M.; Rowlinson, J. S. *J. Chem. Soc., Faraday Trans. 2* **1977**, *73*, 1133–1144.
 (127) Walton, J. P. R. B.; Tildesley, D. J.; Rowlinson, J. S.; Henderson, J. R. *Mol. Phys.* **1983**, *48*, 1357–1368.
 (128) Alejandre, J.; Tildesley, D. J.; Chapela, G. A. *J. Chem. Phys.* **1995**, *102*, 4574–4583.
 (129) Chen, L.-J. *J. Chem. Phys.* **1995**, *103*, 10214–10216.
 (130) Ono, S.; Kondo, S. In *Encyclopedia of Physics*; Flugge, S., Ed.; Springer: Berlin, 1960; Vol. 10.
 (131) Hill, T. L. *Introduction to Statistical Mechanics*; Dover: New York, 1986.
 (132) Given that the ordering of the TTF unit and the DNP ring system are reversed in the case of the amphiphilic rotaxanes (Figure 1f), the dominant factor governing the surface tension is the strength of the nearest neighbor interactions. Consequently, the GSCC has more hydrophobic character because it has a more delocalized π -electron distribution due to strong charge transfer mixing than the MSCC. This insight is corroborated with solubility measurements where it is observed that the GSCC is more soluble in CHCl_3 (1.50 mg/L) than the MSCC (0.96 mg/L) at saturation. It is interesting to note that the proximity of the tetracationic ring and its four hexafluorophosphate counterions to the monolayer's surface does not directly influence the film's hydrophobicity.

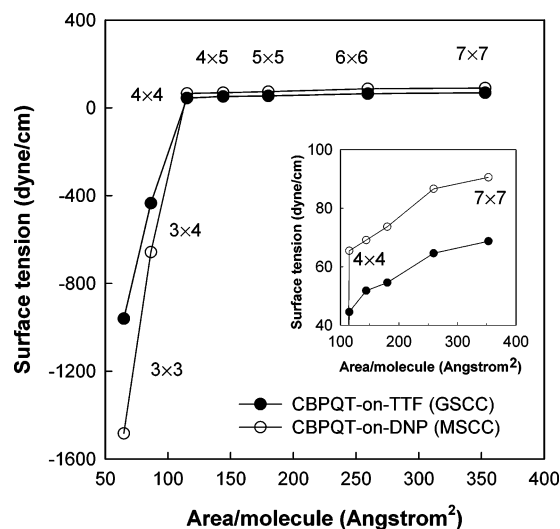


Figure 14. Change of surface tension as a function of the surface coverage for both co-conformations. Inset shows the cases displaying a positive surface tension.

molecule, the value of the water contact angle is larger by $\sim 10^\circ$ for the GSCC than for the MSCC, which is in good agreement with the prediction from the surface tension calculated from the simulations.

Our simulations also revealed that the predicted surface tension increases with increasing area/molecule for both cases as shown in Figure 14 and Table 6. This feature is also observed in our experiments, which reveals that the water contact angle decreases with increasing area/molecule. This agreement in the trend of experimental water contact angle with the calculated surface tension supports the validity of our simulations on the rotaxane SAMs.

For the highly packed case with the 3×3 and 3×4 grid/molecule, we find that both the GSCC and MSCC lead to a *negative* surface tension. Material surfaces with positive surface tension try to reduce the surface free energy by reducing the surface area. Thus, the negative surface tension for the high surface coverage case indicates that the surface wants to expand because the rotaxane molecules are squeezed too tightly against each other due to the over-packing. The negative surface tension becomes less negative rapidly with decreasing surface coverage, becoming positive for the 4×4 grid/molecule ($115 \text{ \AA}^2/\text{molecule}$) coverage and, more so, for lower ones.

4. Conclusions

We have predicted the superstructure and surface properties of a disulfide tethered bistable [2]rotaxane SAM on a Au (111) surface as a function of the surface coverage using atomistic MD simulations. For this purpose, we used the generic Dreiding force field and QEq charges for the nonmetallic atoms, which we showed gives structural and energetic predictions for the noncovalent bonding interaction of the CBPQT $^{4+}$ ring with tetrathiafulvalene unit and with DNP-based systems in excellent agreement with both QM and experiment. We then extended the Dreiding force field to describe the Au-organic nonbond interactions by fitting the QM results on the structure and energetics of ethanethiol chemisorbed on a Au_{32} cluster chosen to mimic the Au (111) surface. In addition, we chose the Au–Au interactions to fit the structure and energetics of FCC Au crystal. The validation of the accuracy of this force field for

these donor–acceptor supramolecular complexes, indicates that it should be useful for other organics on Au and suggests that the same approach could be used to extend these predictions to other metals.

We considered SAMs formed from both the GSCC and MSCC of the bistable rotaxane with various surface coverages to determine the structures and energetics of the rotaxane SAM. For both co-conformations of the rotaxane we find that the most stable SAM has a surface coverage of $115 \text{ \AA}^2/\text{molecule}$ (the 4×4 grid/molecule). We also found that the GSCC is more stable than the MSCC by $\sim 14 \text{ kcal/mol}$ for all favorable surface coverages. This result is in good agreement with the experimental observations.

For the stable SAM structure with surface coverage of $115 \text{ \AA}^2/\text{molecule}$ and smaller, we find that the rotaxanes lead to hexagonal packing. For the lowest coverage of $260 \text{ \AA}^2/\text{molecule}$ we find that the CBPQT $^{4+}$ ring in the SAM lies nearly parallel to the surface for both the GSCC ($\theta = 8^\circ$) and the MSCC ($\theta = 11^\circ$). However, as the surface area decreases the tilt angle of the CBPQT $^{4+}$ ring increases until it is $\theta = 39^\circ$ (GSCC) and $\theta = 61^\circ$ (MSCC) at the optimum coverage. The tilt angle of the entire rotaxane is $\psi = 41^\circ$ (GSCC) and $\psi = 46^\circ$ (MSCC) at the optimum surface coverage. This tilt angle increases up to $\sim 50^\circ$ in the 4×5 grid ($144 \text{ \AA}^2/\text{molecule}$) and then decreases for even smaller surface coverages due to the rotaxane bending downward to fill the newly available space. At the optimum coverage we find a film thickness of 40.5 \AA (GSCC) and 40.0 \AA (MSCC). This SAM thickness decreases with decreasing surface coverage. Over the 2 ns MD simulation we find that the average location of the hexafluorophosphate counterions (PF_6^-) stay coupled with the CBPQT $^{4+}$ ring.

We calculated the surface tension from the stress distributions using the Kirkwood–Buff formula and found that at the optimal packing condition ($115 \text{ \AA}^2/\text{molecule}$, 4×4 grid/molecule) the surface tension is 45 dyn/cm for the GSCC and 65 dyn/cm for the MSCC. Consequently, the predicted higher hydrophobicity for the GSCC relative to that for the MSCC and the decrease of the hydrophobicity with increasing surface area have been confirmed by water contact angle measures on similar self-organized amphiphilic rotaxanes in Langmuir–Blodgett monolayers.

Acknowledgment. The computational work was initiated with support by the National Science Foundation (NIRT, WAG). The collaboration was supported by the Microelectronics Advanced Research Corporation (MARCO, WAG and J.F.S.) and its Focus Centers on Functional Engineered NanoArchitectonics (FENA) and Materials Structures and Devices, the Moletronics Program of the Defense Advanced Research Projects Agency (DARPA, J.F.S. and J.R.H.), the Center for Nanoscale Innovation for Defense (CNID, J.F.S.), the MARCO Materials Structures and Devices Focus Center (J.R.H.). In addition, the facilities of the MSC (WAG) were supported by ONR-DURIP, ARO-DURIP, IBM (SUR), and the Beckman Institute.

Note Added after ASAP Publication. After this article was published ASAP on January 5, 2005, the chemical structures in Figure 1 were corrected. The corrected version was published ASAP on January 11, 2005.

JA044530X